# Adaptive Wavelet Methods for the Navier-Stokes Equations

F. Koster[1], K. Schneider[2], M. Griebel[1], M. Farge[3]
[1] Dept. for Scientific Computing, Universität Bonn; koster{griebel}@iam.uni-bonn.de
[2] Institut für Chemische Technik, Universität Karlsruhe; kschneid@rhrk.uni-kl.de
[3] LMD-CNRS, Ecole Normale Superieure Paris; farge@lmd.ens.fr

## Summary

In this paper we introduce and compare two adaptive wavelet-based Navier Stokes solvers. The first one uses a Petrov-Galerkin vaguelette approach for the vorticity formulation of the Navier stokes equations, while the second one is a collocation method for the pressure-velocity formulation. Both codes are applied to the 2D mixing layer test problem and their results are compared to Fourier spectral solutions.

**Key words.** adaptivity, wavelets, vaguelettes, interpolets, non-linear thresholding

## 1 Introduction

Turbulent flows are characterized by their large number of active scales of motion increasing with the Reynolds number. Hence, for the numerical simulation of fully developed turbulence the complexity has to be considerably reduced and turbulence models are unavoidable. In current approaches the fine scales of the flow are replaced by a subgrid scale model, e.g. in Large Eddy Simulation (LES), using a linear cut–off filter which therefore does not depend on the actual flow realization.

Wavelets are functions with simultaneous localization in physical and in Fourier space which correspond to filters having a constant relative bandwidth. They allow adaptive filtering of signals and are well suited for investigating unsteady, inhomogeneous or intermittent phenomena like those encountered in turbulence.

In the past we have shown that wavelets are an efficient basis to represent turbulent vorticity fields, see *e.g.* [13, 30, 14]. By means of nonlinear filtering of the wavelet coefficients of vorticity, we can separate the dynamical active part of the flow (i.e. the coherent vortices) from the incoherent background flow. This filtering technique is much more efficient than linear low pass filtering employed in LES, because it retains much more enstrophy and energy for the same number of modes.

From a numerical point of view wavelets constitute optimal bases to represent functions with inhomogeneous regularity, such as intermittent turbulent flow fields. The existence of fast pyramidal algorithms (with linear complexity), to transform the computed fields between lacunary wavelet coefficients and structured adaptive grids, allows to design efficient methods for solving nonlinear PDEs [16, 18, 22, 29].

We will present two different wavelet schemes to solve the Navier–Stokes equations. We will compare their performances for computing a two–dimensional temporally growing mixing layer, which is a good test–case because it is a typical configuration encountered in many turbulent flows. The results are compared with those obtained with a classical Fourier pseudo–spectral method.

The remainder of this paper is organized as follows: In the next section we give a brief introduction to wavelets and we present the general adaptive time stepping method which is used by both wavelet solvers. In section three and four further details of the two wavelet schemes are given. In particular the differences between them are pointed out. In section 5 we describe the setup of the mixing layer experiment and we present the results of both schemes compared to Fourier spectral simulations.

## 2 Adaptive Wavelet Methods for Time-Dependent PDEs

In the following, we give a brief introduction to wavelets and our notation used. We first deal with one–dimensional wavelets and then consider two variants for its generalization to the multivariate case. Finally, we describe how wavelets can be used in the adaptive spatial discretization of time stepping methods for e.g convection–diffusion problems or the Navier Stokes equations.

### 2.1 Univariate Wavelets

In this subsection, we explain the main features of our approach in a simple notation using wavelets defined on $\mathbb{R}$. We give brief comments on wavelets on the interval later on.

We start with a sequence of spaces $\{V^l\}_{l \geq l_0}$ which are spanned by dilates/translates of a single function $\phi$. A simple example for $\phi$ is the hat function $\phi(x) = \max(0, 1 - |x|)$. We have

$$V^l = \text{span}\, \mathbf{\Phi}^l, \quad \mathbf{\Phi}^l := \{\phi^{(l,s)}\}_{s \in \mathbb{Z}}\ , \quad \phi^{(l,s)}(x) := \phi(2^l x - s)\ .$$

Here, $l$ denotes the level of refinement and $l_0$ is a certain given coarsest level. The function $\phi$ should have the following properties:

(P1) $\phi$ has compact support or decays sufficiently fast such that it can be truncated. Hence, $|\text{supp}\phi^{(l,s)}| \sim 2^{-l}$.

(P2) There is a $P \in \mathbb{N}$ which depends on the particular $\phi$ such that polynomials of degree less than $P$ can be written as linear combinations of $\{\phi^{(l,s)}\}_{s \in \mathbb{Z}}$ for all $l \geq l_0$. E.g for the hat function we have $P = 2$.

(P3) $\phi$ is the solution of a so-called scaling equation

$$\phi(x) = \sum_{s \in \mathbb{Z}} h_s \phi(2x - s) \tag{2.1}$$

with explicitly known coefficients $\{h_s\}$. Therefore, the functions $\phi$ and $\phi^{(l,s)}$ are called scaling functions. An analytic description of $\phi$ is often not available, but it is also not needed. All we have to know about $\phi$ from the practical point of view are its scaling coefficients $h_s$. An immediate consequence of (2.1) is: $V^l \subset V^{l+1}$.

Now, associated functions, so–called wavelets, can be defined as follows: Wavelets are the basis functions of the complementary spaces $W_l$:

$$V^l = V^{l-1} \oplus W_l \ , \quad W_l = \text{span}\mathbf{\Psi}_l \ , \quad \mathbf{\Psi}_l = \{\psi_{(l,t)}\}_{t\in\mathbb{Z}} \ .$$

In our setting the wavelets are also dilates/translates $\psi_{(l,t)} = \psi(2^l x - t)$ of a single function $\psi$

$$\psi(x) = \sum_{s\in\mathbb{Z}} g_s \phi(2x - s) \ . \tag{2.2}$$

Again, the coefficients $\{g_s\}$ are all what is needed to use $\psi$ and $\psi_{(l,t)}$ in practice. Furthermore, we can assume that $\psi$ also has compact support or decays quite fast. Repeated decomposition of $V^l$ yields a so-called multi-resolution analysis (MRA) of $V^l$ with the wavelet basis $\{\mathbf{\Psi}_l\}_{l\geq l_0}$

$$V^l = \oplus_{k=l_0}^{l} W_k \ , \quad \text{where} \quad W_{l_0} := V^{l_0} \quad \text{and} \quad \mathbf{\Psi}_{l_0} := \mathbf{\Phi}^{l_0}.$$

Consider successive approximations $u^{l-1} \in V^{l-1}$ and $u^l \in V^l$ of a function $u$ and their difference

$$w_l = u^l - u^{l-1} = \sum_{t\in\mathbb{Z}} w_{(l,t)} \psi_{(l,t)} \ .$$

Then, a Taylor argument using (P1) and (P2) shows that the coefficients $w_{(l,t)}$ are significant (i.e. 'large') only if their associated wavelets $\psi_{(l,t)}$ lie in the vicinity of a singularity or a quasi-singularity of $u$. Therefore, for any $u$ which has only a few (quasi-) singularities, the number of active degrees of freedom required to achieve a desired accuracy is substantially less in a wavelet basis compared to a scaling function basis $\mathbf{\Phi}^l$.

The most important analytical property of the wavelet basis is the following: Sobolev norms $||.||_s$ of e.g. $u$ can be characterized in terms of the wavelet coefficients $u_{(l,t)}$: There are $\gamma^* < \gamma$ such that for $s \in ]\gamma^*,\gamma[$ there are $0 < c(s) < C(s)$ with

$$c(s) \sum_{l,t} |u_{(l,t)}|^2 ||\psi_{(l,s)}||_0^2 4^{ls} \ \leq \ ||\sum_{l,t} u_{(l,t)} \psi_{(l,s)}||_s^2 \ \leq \ C(s) \sum_{l,t} |u_{(l,t)}|^2 ||\psi_{(l,s)}||_0^2 4^{ls}. \tag{2.3}$$

Here $\gamma := \sup\{s \mid \phi \in H^s\}$ and $\gamma^*$ mainly depends on the particular basis $\mathbf{\Psi}_l$ of $W_l$. Such norm equivalences are at the heart of the wavelet theory and are also the foundation for efficient preconditioning techniques for linear systems [6, 27, 19, 23] or reliable control of errors [5].

Furthermore, the so–called dual scaling functions $\tilde{\phi}^{(l,s)}$ and the dual wavelets $\tilde{\psi}_{(l,t)}$ can be considered. They have to fulfill the following biorthogonality relations

$$\langle \phi^{(l,s)} \ , \tilde{\phi}^{(l,t)} \rangle = \delta(s-t) \ , \quad \langle \psi^{(k,s)} \ , \tilde{\psi}^{(l,t)} \rangle = \delta(k-l)\delta(s-t) \ .$$

Here, $\langle\ ,\ \rangle$ is usually the $L_2$ scalar product; if the dual functions are linear combinations of Dirac functionals, then $\langle\ ,\ \rangle$ denotes a dual pairing. From the theoretical point of view the dual functions are required for both, the understanding of (2.3) and for the algorithms later on: They can be used as test functions in a Petrov-Galerkin discretization scheme. There, the biorthogonality relations lead to strong simplifications which make programming easy. Again, the dual functions are in general only known by their mask coefficients in scaling relations similar to (2.1) or (2.2).

Note that everything described in this subsection can be generalized to wavelets on an interval $[a,b]$ as well. There, the wavelets and scaling functions, respectively, are defined by appropriately chosen linear combinations of $\{\phi(2^l x - s)\}_{s\in\mathbb{Z}}\chi_{[a,b]}(x)\}$, see [21] and the references therein. In this way it is also possible to incorporate e.g. homogeneous Dirichlet or Neumann boundary conditions required for the solution of PDEs. In case of wavelets on the interval, the spaces $V_l$ and $W_l$ have a finite dimension. More precisely $\dim V^l \approx 2^l$ and $\dim W_l = 2^{l-1}$ $(l > l_0)$.

### 2.2 Multivariate Wavelets

The simplest way to obtain multivariate wavelets is to employ anisotropic or isotropic tensor products:

(MRA-$d$) Here, the multivariate wavelets are defined by

$$\psi_{(\mathbf{l},\mathbf{t})}(\mathbf{x}) := \psi_{(l_1,t_1)}(x_1)\cdot\ldots\cdot\psi_{(l_d,t_d)}(x_d)\ , \quad \mathbf{l} := (l_1,..,l_d)\ ,\ \mathbf{x},\mathbf{t} \text{ analogous.}$$

Note that for certain choices of $\mathbf{l}$, f.e. $\mathbf{l} = (1,..,1,20)$, the support of $\psi_{(\mathbf{l},\mathbf{t})}$ may be very anisotropic.

(MRA) Here, anisotropy is avoided . The wavelets are defined for $\mathbf{e} \in \{0,1\} \times .. \times \{0,1\}\backslash\mathbf{0} \subset \mathbb{N}^d,\ l \geq l_0$ and $\mathbf{t} \in \mathbb{Z}^d$ by

$$\psi_{(\mathbf{e},l,\mathbf{t})} := \psi_{(e_1,l,t_1)}(x_1)\cdot\ldots\cdot\psi_{(e_d,l,t_d)}(x_d)\ ,$$

where $\psi_{(0,l,t)}(x) := \phi^{(l-1,t)}(x)$ and $\psi_{(1,l,t)}(x) := \psi_{(l,t)}(x)$. The size of the support of $\psi_{(\mathbf{e},l,\mathbf{t})}$ is $\sim 2^{-l}$ in each direction, i.e. the basis functions are rather isotropic. The idea behind the above definition can be seen clearly in the 2D case. The scaling functions are simply the tensor products of the univariate scaling functions. Then,

$$\begin{aligned} V^l \otimes V^l &= (V^{l-1} \oplus W_l) \otimes (V^{l-1} \oplus W_l) \\ &= V^{l-1} \otimes V^{l-1} \\ &\quad \oplus (W_l \otimes V^{l-1})\ \oplus\ (V^{l-1} \otimes W_l)\ \oplus\ (W_l \otimes W_l)\ . \end{aligned}$$

Obviously, $V^l \otimes V^l$ plays the role of $V^l$ in the one–dimensional case and $V^{l-1} \otimes V^{l-1}$ plays that of $V^{l-1}$. Hence, $(W_l \otimes V^{l-1})\ \oplus\ (V^{l-1} \otimes W_l)\ \oplus\ (W_l \otimes W_l)$ plays the role of $W_l$.

In case of the (MRA)-approach we have a linear order of the approximation spaces $\left( V^{l-1} \otimes .. \otimes V^{l-1} \subset V^{l} \otimes .. \otimes V^{l} \right)$ similar to the one–dimensional case while for the (MRA-$d$)-approach the underlying approximation spaces $V^{\mathbf{l}} = V^{l_1} \otimes .. \otimes V^{l_d}$ form a $d$–dimensional array [27]. This explains our naming convention (MRA$\{$-$d\}$).

The constructions for the dual scaling functions/wavelets are the same as for the (primal) scaling functions/wavelets.

To unify the notation we denote by $\psi_\lambda$ and $u_\lambda$ the wavelets and the wavelet coefficients for both, the (MRA-$d$)- and the (MRA)-approach. In the first case $\lambda = (\mathbf{l},\mathbf{t})$ and in the second case $\lambda = (\mathbf{e},l,\mathbf{t})$.

A problem closely related to the efficiency of adaptive methods is the best $N$-term approximation for a given function $v$. Here, one is interested in the order $\alpha(v,s)$ such that for all $N \in \mathbb{N}$ and a suitable constant $C$ independent of $N$ there holds

$$\inf \Big\{ \|v - \sum_{\lambda \in \mathcal{T}} v_\lambda \cdot \psi_\lambda\|_s \;\Big|\, \boldsymbol{\mathcal{T}} \text{ and } \{v_\lambda\}_{\lambda\in\mathcal{T}} \text{ arbitrary, but } \#\boldsymbol{\mathcal{T}} = N \Big\} \;\leq\; CN^{-\alpha}. \quad (2.4)$$

Since we can represent each $\phi^{(l,s)}$ by $O(l)$ wavelets $\psi_{(k,t)}$ the order $\alpha_{MRA-d}$ for the (MRA-$d$)-approach is at least arbitrarily close to the order $\alpha_{MRA}$ for the (MRA)-approach. Of course the constant $C_{MRA-d}$ may be substantially different from $C_{MRA}$. However, the point is that under some relatively mild assumptions on the smoothness of $u$, the (MRA-$d$)-approach yields a significantly larger order of approximation than the (MRA)-approach: $\alpha_{MRA-d} > \alpha_{MRA}$. Further information on this topic can be found in e.g. [27, 10, 9, 17, 34].

Finally, some comments on the geometry of the considered domain are in order. Due to the intrinsic tensor product construction of both multivariate approaches, rectangular domains are the only geometries for which the (MRA-$d$)- and the (MRA)-wavelets can be used directly. Thus, complicated geometries pose a serious problem.

With respect to the implementational effort, the simplest solution is to embed a given non-rectangular domain $\Omega \subset \mathbb{R}^d$ into an enclosing rectangular domain and to solve here a modified PDE, where the boundary conditions on $\partial\Omega$ are included in the right hand side. See [12] and the references therein for the special case of the Navier-Stokes equations. However, a drawback of this approach is the additional adaptive refinement needed in the vicinity of $\partial\Omega$ in order to resolve the forcing term sufficiently accurate.

Another solution to the geometry problem is the use of parametric mappings, i.e. the computational domain $[0,1]^d$ is mapped to the real domain $\Omega$. Topological complicated situations are handled by structured blocks. This approach is quite common in engineering applications. In context of the Navier Stokes equations this approach has a further advantage: The underlying curvilinear grid is aligned to the surface of $\Omega$. Now, since the flow is approximately also aligned to the surface of $\Omega$, the flow is approximately aligned to the underlying grid. This is exactly the situation where we can expect the (MRA-$d$)-approach to work very well.

### 2.3 Time Dependent Problems and Adaptive Basis Selection

Consider the linear convection-diffusion problem

$$\begin{aligned} \partial_t a + \nabla\cdot(\mathbf{v}a) &= \nu\Delta a\,, \quad (\mathbf{x},t)\in\Omega\otimes[0,T]\,, \\ a(\mathbf{x},0) &= a^0(\mathbf{x})\,, \end{aligned} \tag{2.5}$$

which is a model for the evolution part of the Navier Stokes equations. A common way to discretize (2.5) is to use a FD/E/V or wavelet method for the spatial discretization and a time stepping (i.e. FD) method for the time discretization:

$$\frac{a^{n+1}-a^n}{\Delta t} + C(a^n,a^{n-1},..) = \nu\Delta a^{n+1}. \tag{2.6}$$

Here, $C(.)$ is an explicit approximation to the convective term e.g. of Adams-Bashforth or Runge-Kutta type. Note that in case of strongly time-dependent problems like turbulence (our final goal) the additional effort for the implicit treatment of the convective term does not pay off, since the time step size $\Delta t$ has to be quite small anyway.

An important question for our adaptive wavelet methods is how to select the adaptive basis. A simple, but efficient strategy is the following:
For the initial condition $a^0$ we use an appropriately chosen initial adaptive basis $\{\psi_\lambda\}_{\lambda\in\boldsymbol{\mathcal{T}}^0}$. Usually $\boldsymbol{\mathcal{T}}^0$ is the set of $\lambda$ with $l$ or $|\mathbf{l}|_\infty$ less than a maximum level $L$. Then, the time evolution of $a$ and $\boldsymbol{\mathcal{T}}$ is calculated as follows:

**(Adaptive Time Stepping Method)**

given are the initial adaptive index set $\boldsymbol{\mathcal{T}}^0$ and $a^0_{\boldsymbol{\mathcal{T}}^0} = \sum_{\lambda\in\boldsymbol{\mathcal{T}}^0} a^0_\lambda \cdot \psi_\lambda$

`for` $n=0$ `to` $T/\Delta t$ `do`

`// Time Step:`

Calculate the convective term $C^n_{\boldsymbol{\mathcal{T}}^n}$

Solve $(I - \Delta t\nu\Delta)a^{n+1}_{\boldsymbol{\mathcal{T}}^n} = a^n_{\boldsymbol{\mathcal{T}}^n} - \Delta t C^n_{\boldsymbol{\mathcal{T}}^n}$

`// Adaptivity: new adaptive basis`

Determine $\overline{\boldsymbol{\mathcal{T}}}^{n+1} := \{\ \lambda\in\boldsymbol{\mathcal{T}}^n \ \mid\ |a^{n+1}_\lambda| > \epsilon\}$

Determine $\boldsymbol{\mathcal{T}}^{n+1} := \{\mu \mid \exists\ \lambda\in\overline{\boldsymbol{\mathcal{T}}}^{n+1}$ such that $dist(\mu,\lambda)\le R\}$

`// Adaptivity: prolongation to new basis`

Set $a^{n+1}_{\boldsymbol{\mathcal{T}}^{n+1}} := \sum_{\lambda\in\boldsymbol{\mathcal{T}}^{n+1}\bigcap\boldsymbol{\mathcal{T}}^n} a^{n+1}_\lambda\cdot\psi_\lambda$

`end`

The first part of this algorithm is the time stepping method (2.6). Here, we used an Euler scheme for the sake of simplicity. Note however, that other higher order time discretization methods can be plugged in straightforwardly.

In the second part, first we determine the set $\overline{\mathcal{T}}^{n+1}$ of active basis functions. The analog of this step in adaptive FE/V methods would be the selection of elements which should be refined. The refinement criterion we use is whether or not the magnitude of a particular wavelet coefficient is larger than a given threshold, i.e. $|a_\lambda| > \epsilon$. [1]

The use of the magnitude of the wavelet coefficients can also be interpreted as a traditional method of local error estimation. If one takes (P1) and (P2) into account it is quite easy to see that the magnitude of a wavelet coefficient $a_\lambda$ is a measure of the magnitude of a local finite difference approximation of some higher order derivative of $a$, i.e. we work with a gradient type error indicator.

Now consider the second step of the adaptivity strategy, i.e. the determination of $\mathcal{T}^{n+1}$ by insertion of basis functions which are in space and scale close to the active basis functions of $\overline{\mathcal{T}}^{n+1}$. We assume that the current solution $a^n$ is quite accurate and we want to preserve this property also for the next time slice $a^{n+1}$. For the sake of simplicity, let us assume that we calculate $a^{n+1}$ by the following explicit Petrov–Galerkin scheme:

$$\langle a^{n+1} \, , \, \tilde{\psi}_\lambda \rangle = \langle (I - \Delta t \nabla \cdot (\mathbf{v}.) + \Delta t \nu \Delta) a^n \, , \, \tilde{\psi}_\lambda \rangle \, .$$

The best index set $\mathcal{T}^{n+1}$ with a given number $N$ of degrees of freedom is that with the $N$ largest entries $\langle a^{n+1} \, , \, \tilde{\psi}_\lambda \rangle$. Now, the a priori known locality properties of the differential operator $(I - \Delta t \nabla \cdot (\mathbf{v}.) + \Delta t \nu \Delta)$ show that $\langle a^{n+1} \, , \, \tilde{\psi}_\lambda \rangle$ can only be significant if $\lambda$ is near to one of the significant $\mu \in \mathcal{T}^n$. In this sense, the above method is closely related to the works of Cohen, Dahmen and DeVore [5] or the work of Becker and Rannacher [1, 2].

The last issue of the section is the conservation of mass or energy. We may assume that the wavelets $\psi_\lambda$ have a vanishing mean value, except for the wavelets on the coarsest level which are always kept in the adaptive basis. Then, the remeshing step does not change the mass budget $\int_\Omega a d\mathbf{x}$. Unfortunately, things are more complicated for the energy $\int a^2 d\mathbf{x}$. For $L_2$-orthogonal wavelets (which are used in method I described in the next section) there is no problem, but for all other types of wavelet-approaches we usually have only an estimate for the change of energy (see eq. (2.3)) introduced by the remeshing step. Of course this change will be quite small, but we can not say whether the energy defect is positive or negative.

However, in our numerical experiments [23] with non-$L_2$-orthogonal Interpolet wavelets (see section 4) it turned out that the dominant contribution of the energy defect does not come from remeshing but from the discretization of the convective term which is not energy conservative in the adaptive case, since telescope or partial summation arguments fail. Nevertheless, we observed a very good prediction of the rate of energy dissipation. Figure 1 shows the energy and the number of degrees of freedom (DOF) for the Molenkamp test of a rotating hill (see e.g. [24] pp. 248) with the quite small diffusion of $\nu = 10^{-5}$, i.e $Re = 10^5$, using (MRA-$d$)-Interpolet wavelets.

[1] Another possible strategy would be to choose the $N$ largest wavelet coefficients, where $N$ is a fixed given number. In this case the work count would be almost constant for all time steps.

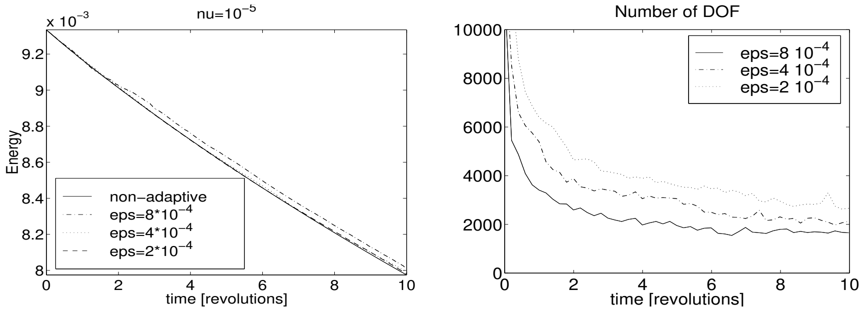


**Figure 1** DOF and energy for adaptive Molenkamp test. The maximum #DOF for ($\epsilon = 2_{-4}$) is $\approx 17000$.

## 3 Method I

For the numerical simulation of two–dimensional turbulence we consider the Navier–Stokes equations written in velocity–vorticity formulation

$$\partial_t \omega + \mathbf{v} \cdot \nabla \omega = \nu \nabla^2 \omega \;, \qquad \nabla \cdot \mathbf{v} = 0 \;, \tag{3.7}$$

with the velocity field $\mathbf{v} = (u,v)$, the vorticity $\omega = \nabla \times \mathbf{v}$ and the kinematic viscosity $\nu$. We assume periodic boundary conditions in both directions.

For the time discretization we use finite differences with a semi–implicit scheme, i.e. backward-Euler for the viscous term and Adams–Bashforth extrapolation for the nonlinear term, both of second order. We obtain

$$(\gamma I - \nu \nabla^2)\omega^{n+1} = \frac{4}{3}\gamma\omega^n - \frac{1}{3}\gamma\omega^{n-1} - \mathbf{v}^\star \cdot \nabla\omega^\star, \text{ where } \omega^\star = 2\omega^n - \omega^{n-1} \tag{3.8}$$

with time step $\Delta t$, $\gamma = 3/(2\Delta t)$ and $I$ representing the identity.

For the spatial discretization we use a Petrov–Galerkin scheme. Therefore the vorticity is expanded into a set of trial functions and the minimization of the weighted residual of (3.8) requires that the projection onto a space of test functions vanishes.

As space of trial functions we employ a multiresolution analysis in two dimensions, i.e. the (MRA)-approach, and expand $\omega^n$ at time step $n$ into an orthonormal wavelet series, from the largest scale $l_{max} = 2^0$ to the smallest scale $l_{min} = 2^{-L}$:

$$\omega^n(x,y) = \sum_{l=0}^{L} \sum_{\mathbf{e}} \sum_{\mathbf{t}} \omega_\lambda^n \psi_\lambda(x,y) \;, \quad \text{where } \lambda = (\mathbf{e},l,\mathbf{t}) \;. \tag{3.9}$$

Here, the wavelets $\psi_\lambda$ stem from one–dimensional orthogonal wavelets [7] with periodic boundary conditions. Thus, the wavelets $\psi_\lambda$ also form a $L_2$-orthogonal basis, i.e.

$$\langle \psi_\lambda \,,\, \psi_\mu \rangle = \delta(\lambda - \mu) \;.$$

One consequence of this is that we know exactly what amount of enstrophy is lost in the remeshing step.

The test functions $\theta_\mu$ used for the transport equation are then defined as solutions of the linear part of equation (3.8), i.e.

$$(\gamma I - \nu \nabla^2)\theta_\mu \;=\; \psi_\mu \; . \tag{3.10}$$

Hence,

$$\langle (\gamma I - \nu \nabla^2)\psi_\lambda \, , \, \theta_\mu \rangle = \langle \psi_\lambda \, , \, (\gamma I - \nu \nabla^2)\theta_\mu \rangle = \delta(\lambda - \mu) \; .$$

This avoids the assembly of the stiffness matrix and the solution of a linear equation at each time step. The functions $\theta_\mu$, called vaguelettes, are explicitly calculated in Fourier space and have localization properties similar to wavelets.

The solution of (3.8) therewith reduces to a simple change of basis,

$$\omega_\lambda^{n+1} \;=\; \langle \omega^{n+1} \, , \psi_\lambda \rangle \;=\; \langle \frac{4}{3}\gamma\omega^n - \frac{1}{3}\gamma\omega^{n-1} - \mathbf{v}^\star \cdot \nabla\omega^\star \, , \, \theta_\lambda \rangle \; . \tag{3.11}$$

An adaptive discretization is obtained by the *Adaptive Time Stepping Method* of the previous section using a nonlinear wavelet thresholding technique which retains only wavelet coefficients $\omega_\lambda^n$ with absolute value above a given threshold $\epsilon = \epsilon_0 \sqrt{Z}$, where $Z \;=\; \frac{1}{2} \int \omega^2 dx$. The nonlinear term $\mathbf{v}^\star \cdot \nabla\omega^\star$ is evaluated by partial collocation on a locally refined grid. The vorticity $\omega^\star$ is reconstructed in physical space on an adaptive grid from its wavelet coefficients $\{\omega_\lambda^\star\}$ using the adaptive wavelet reconstruction algorithm [3]. Using the adaptive vaguelette decomposition with $\theta \;=\; (\nabla^2)^{-1}\,\psi$, we solve $\nabla^2\Psi^\star \;=\; \omega^\star$ ($\Psi^\star$ being the stream function), get $\{\Psi_\lambda^\star\}$ and finally reconstruct $\Psi^\star$ on the refined grid. By means of centered finite differences of 4th order we finally compute $\nabla\omega^\star$ and $\mathbf{v}^\star \;=\; (-\partial_y \Psi^\star, \partial_x \Psi^\star)$ on the adaptive grid and we evaluate the nonlinear term pointwise. Subsequently (3.11) can be solved using the adaptive vaguelette decomposition. A complete description of this algorithm is given in e.g. [29]. Finally let us mention that the total complexity of the algorithm is of order $O(N_{ad})$, where $N_{ad}$ denotes the number of wavelet coefficients retained in the adapted basis.

# 4 Method II

For this method we used Deslaurier-Dubuc Interpolets [8, 22] together with the (MRA-$d$) construction and their dual counterparts as trial and test functions. The advantage of Interpolets is that not only the scaling functions, but also the wavelets are interpolating. This allows for the efficient evaluation of non-linear terms. Besides of its potential advantages with respect to an efficient approximation (2.4), the (MRA-$d$) technique leads to a very simple structure of the algorithms in the multivariate case: All operations we require (adaptive wavelet transform, its inverse, the adaptive evaluation of differential operators) boil down to the corresponding adaptive operations for the 1D case. As an example we consider the evaluation of the $\partial_{xx}$ part of the Laplacian:

$$\langle \partial_{xx} \sum_{\mathbf{k},\mathbf{s}} a_{(\mathbf{k},\mathbf{s})} \psi_{(\mathbf{k},\mathbf{s})} \, , \tilde{\psi}_{(\mathbf{l},\mathbf{t})} \rangle =$$

$$
\begin{aligned}
&= \sum_{\mathbf{k},\mathbf{s}} a_{(\mathbf{k},\mathbf{s})} \langle \partial_{xx} \psi_{(k_1,s_1)} \, , \, \tilde{\psi}_{(l_1,t_1)} \rangle \cdot \prod_{i=2}^{d} \delta(k_i - l_i) \delta(s_i - t_i) \\
&= \langle \partial_{xx} \sum_{k,s} a_{((k,l_2,..,l_d),(s,t_2,..,t_d))} \psi_{(k,s)} \, , \, \tilde{\psi}_{(l_1,t_1)} \rangle \, .
\end{aligned}
$$

A description of the complete scheme and of all adaptive algorithms is given in [22]. These algorithms have a work count which is proportional to $\#\mathcal{T}$. An analysis of the consistency order of the Interpolet Petrov-Galerkin scheme is contained in [20].

Now, we consider the Navier-Stokes equations in primitive variable formulation:

$$
\begin{aligned}
\partial_t \mathbf{v} + \nabla(\mathbf{v} \otimes \mathbf{v}) &= \mathbf{f} - \nabla p + \nu \Delta \mathbf{v} \\
\nabla \cdot \mathbf{v} &= 0 \\
\mathbf{v}(\mathbf{x},0) &= \mathbf{v}^0(\mathbf{x}) \quad ,
\end{aligned}
$$

with appropriate boundary conditions. The time discretization is achieved by means of a Chorin-type projection method:

(Transport step)
$$
\frac{\bar{\mathbf{v}}^{n+1} - \mathbf{v}^n}{\Delta t} + \mathbf{C}(\mathbf{v}^n, \mathbf{v}^{n-1}, ..) = \mathbf{f}^{n+1} - \nabla p^n + \nu \Delta \bar{\mathbf{v}}^{n+1} \tag{4.12}
$$

(Projection step)
$$
\begin{aligned}
\frac{\mathbf{v}^{n+1} - \bar{\mathbf{v}}^n}{\Delta t} &= -\nabla(p^{n+1} - p^n) \qquad (4.13) \\
\nabla \cdot \mathbf{v}^{n+1} &= 0
\end{aligned}
$$

The projection step involves a saddle problem which can be treated by solving

$$
\nabla \cdot \nabla(p^{n+1} - p^n) = \frac{1}{\Delta t} \nabla \cdot \bar{\mathbf{v}}^{n+1}
$$

with appropriate boundary conditions for the pressure. If periodic boundary conditions are prescribed for the velocity, then $\bar{\mathbf{v}}$ and $p$ have periodic boundary conditions. If Dirichlet boundary conditions $\mathbf{v}_D$ are prescribed for $\mathbf{v}$, then these boundary conditions are also used for $\bar{\mathbf{v}}$ and homogeneous Neumann boundary conditions are used for $p$ to ensure that $\mathbf{v} \cdot \mathbf{n} = \mathbf{v}_D \cdot \mathbf{n}$ on $\partial\Omega$ at least. There is a controversy about Neumann boundary conditions for $p$ in the literature (see e.g. [15] sec. 3.8.2) but at least for boundary layer flows they are the physically correct ones. For all other cases we can use the modified projection method of [28] which overcomes the problems of the Neumann boundary conditions.

All boundary conditions are implemented by employing Interpolet–wavelets as trial functions which fulfill the boundary conditions.

The convective term is discretized using a 3rd order Adams-Bashforth scheme.

The operator $\nabla \cdot \nabla$ in the pressure Poisson equation requires special attention. Instead of the usual discrete Laplacian this operator is the nested application of the discrete gradient operator for the pressure and the discrete divergence operator for the velocity. Only this structure ensures that the velocity $\mathbf{v}^{n+1}$ is discretely divergence-free after the projection step. A drawback of this operator is that it is not spectrally equivalent to the continuous Laplacian. Spurious pressure oscillations and the breakdown of the efficiency of the usual diagonal wavelet preconditioner are the result. In particular it can be shown by the techniques of [22] (sec. 6) that the condition number of the preconditioned operator is $O(4^L 2^{(d-1)L/2})$ if $L$ is the finest level appearing in the adaptive index set $\boldsymbol{\mathcal{T}}$ and $d$ the dimension of $\Omega$, i.e. $d = 2{,}3$. A solution to this problem is to slightly modify (see [22]) both, the discrete gradient operator for the pressure and the discrete divergence operator for the velocity. Then, the spectral equivalence with the continuous Laplacian is established and the diagonal preconditioner yields a condition number of $O(2^{(d-1)L/2})$. This can be further improved to $O(1)$ by employing a more sophisticated technique (see [22] sec. 6) which is based on the lifting scheme. However, at least for the numerical experiments of the next section the latter improvement was not necessary, since the number of iterations of the BiCGStab solver were quite low: between 2-4 in each time step for the pressure Poisson equation and between 1-2 for the transport equations.

## 5 Numerical Experiments

We consider a temporally developing mixing layer [25], schematically sketched in Fig. 2. The initial velocity has a hyperbolic–tangent profile $u(y) = U \tanh(2y/\delta_0)$ which implies a vorticity thickness $\delta_0 = 2U/(du/dy)|_{y=0}$. From linear stability analysis the mixing layer is known to be inviscidly unstable. A perturbation leads to the formation of vortices by Kelvin–Helmholtz instability, where the most amplified mode corresponds to a longitudinal wavelength $\lambda = 7\delta_0$ [26].

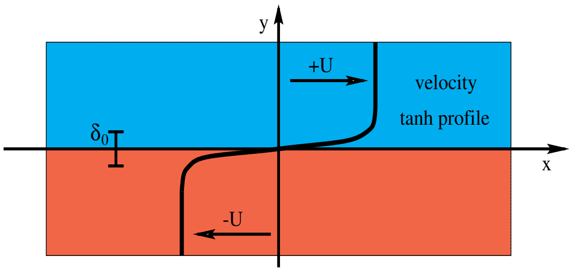


**Figure 2** Initial configuration for the mixing layer.

The initial vorticity thickness $\delta_0$ is chosen such that 10 vortices should develop in the numerical domain of size $[0,2\pi]^2$. To trigger the instability we superimposed a weak white noise in the rotational region. The velocity is $U \approx 0.1035$ and the viscosity is $\nu = 5 \cdot 10^{-5}$.

For the reference simulations two Fourier spectral codes were applied to the periodized version of the problem with two mixing layers on $[0,2\pi] \times [0,4\pi]$. The first code is based on the vorticity formulation of the Navier-Stokes equations and employs a 2nd order Adams-Bashforth (AB2) scheme as in method I; the second code is based on the pressure-velocity formulation and uses a 3rd order Adams-Bashforth (AB3) scheme as in method II. The numerical resolution was $256 \times 512$ for both codes.

### 5.1 Results for method I

For the numerical simulation we employ a maximal resolution of $256 \times 256$, which corresponds to $L = 8$ in (3.9), and cubic spline wavelets of Battle–Lemarié type. The time step is $\Delta t = 2.5 \cdot 10^{-3}$. The threshold for the wavelet coefficients was $\epsilon_0 = 10^{-6}$.

In Fig. 3 (left) we compare the energy spectrum at $t = 37.5$ for a reference computation using a classical pseudo-spectral method, and for two wavelet computations using different thresholds ($\epsilon_0 = 10^{-6}$ and $10^{-5}$).

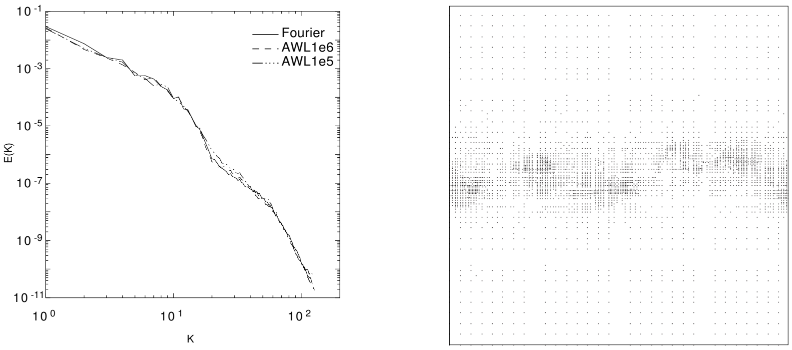


**Figure 3** Left: energy spectra for the pseudo–spectral reference run and for the adaptive wavelet simulations with thresholds $\epsilon_0 = 10^{-6}, 10^{-5}$. Right: adaptive grid reconstructed from the index set of the retained wavelet coefficients. Both at time $t = 37.5$.

Fig. 3 (left) shows that all scales of the flow are well–resolved for both thresholds. The underlying grid Fig. 3 (right) which corresponds to the centers of active wavelets for the computation with $\epsilon_0 = 10^{-6}$ at $t = 37.5$ shows a local refinement in regions of strong gradients where dissipation is most active. In Fig. 4 (bottom) we show the evolution of the vorticity field for the adaptive wavelet simulation with threshold $\epsilon_0 = 10^{-6}$ and for the reference pseudo–spectral computation (top). In both simulations, as predicted by the linear theory, 10 vortices are formed, which subsequently undergo successive mergings. In Fig. 5 the active wavelet coefficients (gray entries) are plotted using a logarithmic scale. The coefficients $\omega(\mathbf{e},l,\mathbf{t})$ are placed at position $(x_1,x_2)$, $x_i = 2^{l-1} \cdot e_i + t_i$ with the origin in the lower left corner and the $y$-coordinate oriented upwards, from coarser to finer scales. We observe that the basis dynamically adapts to the flow evolution during the computation with only $8\%$ of the coefficients being used. We observe that in the wavelet simulation the formation and evolution of vortices

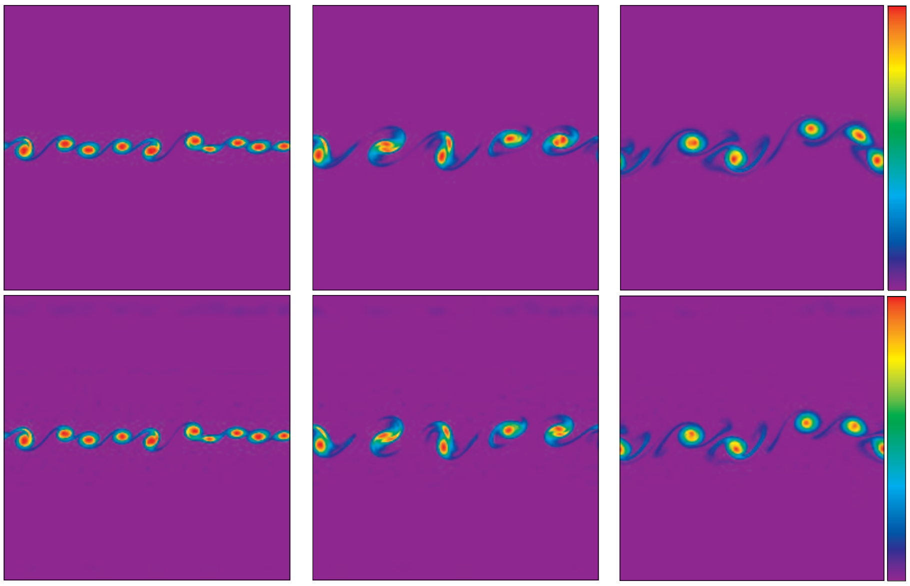

**Figure 4** $|\omega|$ at $t = 12.5,\ 25,\ 37.5$. Top: spectral (vorticity-based). Bottom: method I ($\epsilon_0 = 1_{-6}$).

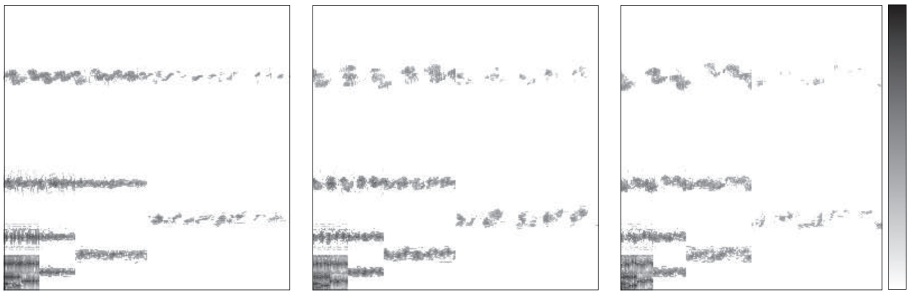

**Figure 5** Active wavelet coefficients at $t = 12.5,\ 25,\ 37.5$. Method I ($\epsilon_0 = 1_{-6}$).

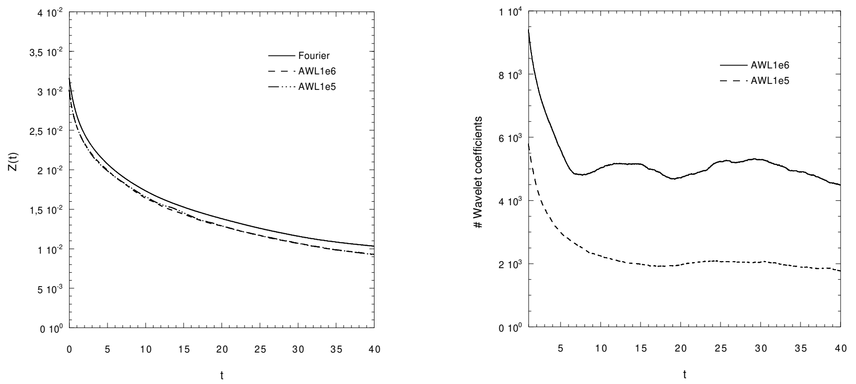


**Figure 6** Left: evolution of enstrophy. Right: evolution of #DOF. Method I ($\epsilon_0 = 1_{-6}, 1_{-5}$).

are well captured, although we find that at later times a slight phase shift appears with respect to the reference run (top). This might be due to the fact that the retained wavelet coefficients contain 94% of the total enstrophy, as observed in Fig. 6 (left) which shows the time evolution of the total enstrophy using the different thresholds. The 6% loss of enstrophy comes from the fact that in the wavelet simulations we have not modelled the effect of the discarded modes onto the retained ones, similarly to the subgrid scale model used in LES. This will be considered in future work, where the enstrophy of the discarded wavelets will be reinjected into the coherent vortices using the wavelet forcing method we have proposed [32].

Another explanation for the phase shift might be that the method discretizes the most important term, i.e. the convective term, by central finite differences. Therefore, the method behaves like a central finite difference method. It is well known [4] that in this case the phase error is the dominating error.

Finally, we plot the time evolution of the number of degrees of freedom for the two wavelet runs in Fig. 6 (right). First, we observe an initial phase, up to $t = 7$ s, where there is a strong reduction in the number of active modes, which corresponds to the formation of the coherent vortices. Then the number of active modes remains almost constant, and represent a significant reduction of the number of modes, with $N_{ad} = 5000$ for $\epsilon_0 = 10^{-6}$ and $N_{ad} = 2000$ for $\epsilon_0 = 10^{-5}$ out of $N = 65536$ initial modes.

### 5.2 Results for Method II

For the numerical simulations we employed tensor products of 6th order Interpolets, i.e. $P = 6$ in (P2), see section 2. The values of the threshold parameter $\epsilon$ were set to $\{12, 8, 4\} \cdot 10^{-4}$. Note that these values can not be directly compared to $\epsilon_0 = 10^{-6}$ used in method I, since there, the wavelets are normalized to $||\psi_{(\mathbf{e},l,\mathbf{t})}|| \sim 1$, while the Interpolet wavelets are normalized to $||\psi_{(\mathbf{l},\mathbf{t})}||_0 \sim 2^{-(l_1+..+l_d)/2}$. If we would normalize them to $\sim 1$ then, the present threshold criterion corresponds to $|u_{(\mathbf{l},\mathbf{t})}| \cdot 2^{(l_1+..+l_d)/2} > \epsilon$, i.e. finer scales get a larger weight. This can be generalized to criteria of type:

$$|u_\lambda| \cdot f(\lambda) > \epsilon, \text{ with e.g. } \quad f(\mathbf{l},\mathbf{t}) = 2^{(l_1+..+l_d)/2}\left(4^{sl_1} + ... + 4^{sl_d}\right) .$$

In this case the threshold strategy is adjustable to different Sobolev norms by the parameter $s$ (compare (2.3)). Numerical experiments with respect to the impact of $f$ to the performance of the adaptive scheme will be done in the future.

In the present numerical experiments with method II the finest level $\mathbf{l}$ was $(9{,}10)$ to take into account the expected anisotropy of the mesh. The time step was $\Delta t = 10^{-2}$ which corresponds to a CFL number of $\approx 0.2$ with respect to the maximum velocity encountered during the simulation. The initial velocity has been calculated in Fourier space with $512 \times 1024$ modes from the initial vorticity field used for method I.

In Figure 7 we give the results for the velocity-based spectral code (top) and method II (bottom). Both results agree very well. Only for $t = 37.5$ there is a phase shift for the right most two vortices. Despite of these slight differences in the instantaneous vorticity fields, the agreement between the spectral and the adaptive solutions with respect to the statistical quantity enstrophy $Z = 0.5 \int \omega^2 d\mathbf{x}$ is almost perfect as shown in Figure 9

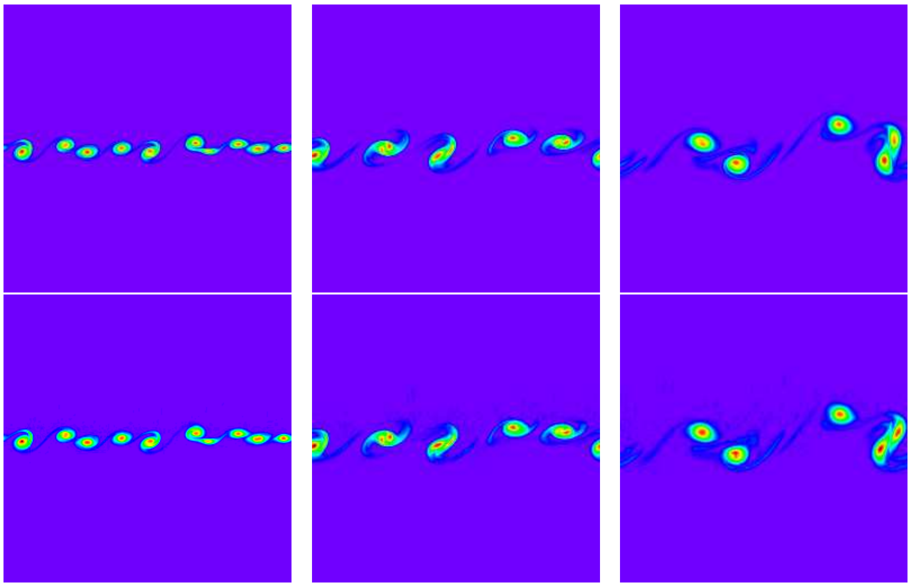

**Figure 7** $|\omega|$ at $t = 12.5, 25, 37.5$. Top: spectral (velocity-based). Bottom: method II ($\epsilon = 8_{-4}$).

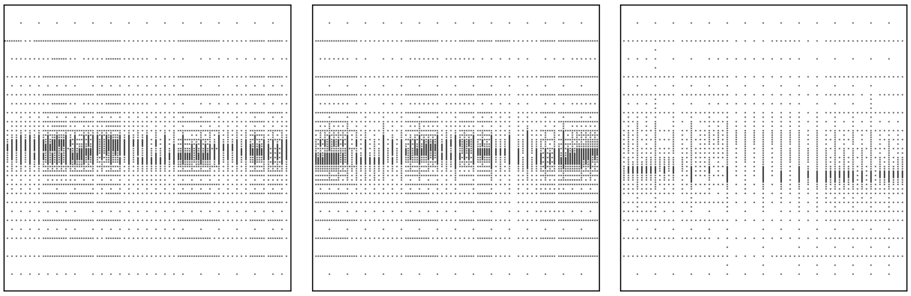

**Figure 8** Adaptive grids $t = 12.5, 25, 37.5$. Method II ($\epsilon = 8_{-4}$).

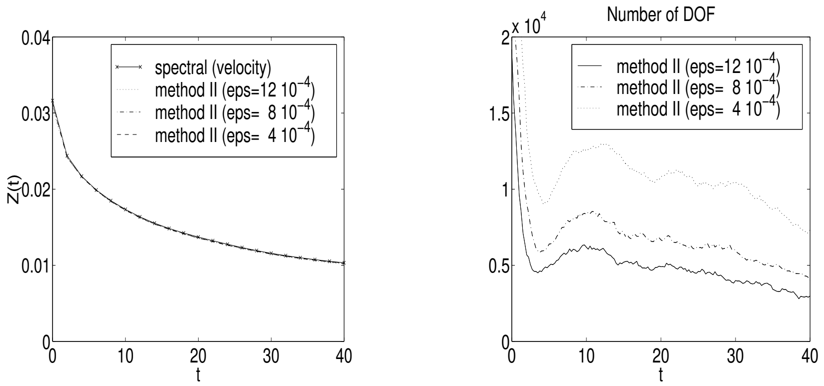


**Figure 9** Left: evolution of enstrophy. Right: evolution of #DOF. Method II. The maximum #DOF for ($\epsilon = 4_{-4}$) is $\approx 31000$.

(left). Note that we calculated the enstrophy only for $t = 0, 2, 4,$ ... This explains the kink at $t = 2$.

The evolution of the number of degrees of freedom (DOF) is shown in Figure 9 (right). The initial velocity is not very smooth because of the white noise added to trigger the instability. Therefore, a large number of DOF is required to resolve the initial velocity sufficiently well. Then, in a first phase the diffusion smooths the velocity very fast which leads to the strong decay of the number of DOF. This process is stopped by the development of the Kelvin-Helmholtz instabilities leading to an increase of the number of DOF ($4 < t < 10$). In the last phase ($t > 10$) the number of coherent vortices constantly decreases by successive merging. (The final state are two counter-rotating vortices which dissipate.) Therefore, in this stage the number of DOF decreases almost constantly.

In Figure 8 adaptive grids are shown which are associated to the adaptive index sets $\mathcal{T}$. Each $(\mathbf{l},\mathbf{t}) \in \mathcal{T}$ corresponds to the node $(x_1,x_2)$, $x_i = 2^{-l_i}t_i$.

## 6 Conclusion

We have shown that the two different adaptive wavelet methods presented here yield reliable and very accurate results with a quite small number of degrees of freedom. Although method I and II are Eulerian and are based on Petrov-Galerkin schemes, their adaptive character in both space and scale allows us to track the displacements and deformations of active flow regions as Lagrangian methods would do. These methods can also be applied to compute other flow configurations, such as jets or wakes, where coherent vortices play an important dynamical role.

Note that with respect to the instantaneous vorticity fields the results of method I and II and their reference codes, respectively, differ significantly. In our opinion this is due to the different spatial discretizations inherent in a vorticity- or velocity-formulation of the Navier-Stokes equations and, consequently, the slightly different initial conditions. We made further experiments with the velocity-based spectral solver and varied the time step $\Delta t$ and also changed the time discretization from AB3 to AB2, but the results were practically the same as those shown in Figure 7. This shows that the reason for the difference between Figure 4 and Figure 7 is not the different time discretization (AB2 and AB3).

## References

[1] Becker R., Rannacher R., *Weighted a posteriori error control in FE methods*; in ENUMATH-95 in Proc. ENUMATH-97, World Scientific Publ., Singapore (1998)

[2] Becker R., *Weighted error estimators for FE approximations of the incompressible Navier-Stokes equations*; to appear in Comput. Methods Appl. Mech. Engrg. (1998)

[3] Bockhorn, H., Fröhlich, J. and Schneider, K., *An adaptive two–dimensional wavelet–vaguelette algorithm for the computation of flame balls*; Combust. Theory Modelling 3 (1999) 177–198.

[4] Canuto C., Hussaini M., Quarteroni A., Zang T., *Spectral Methods in Fluid Dynamics*; Springer Verlag (1988)

[5] Cohen A., Dahmen W., DeVore R., *Adaptive wavelet methods for elliptic operator equations - convergence rates* IGPM-Report, (1998), RWTH Aachen

[6] Dahmen W., *Wavelet and Multiscale Methods for Operator Equations*; Acta Numerica 6 (1997) pp.55-228

[7] Daubechies I., *Ten lectures on wavelets*; Regional Conference Series in Appl. Math. 61 (1992)

[8] Deslaurier G., Dubuc S., *Symmetric iterative interpolation processes*; Constr. Appr. 5 (1989), pp. 49-68

[9] DeVore R., *Nonlinear Approximation*; Acta Numerica 8 (1999)

[10] DeVore R., Konyagin S.V., Temlyakov V.N., *Hyperbolic wavelet approximation*; Constr. Approx. 14 (1998), pp. 1-26

[11] Donoho D., *Interpolating wavelet transform*; Stanford University (1992), preprint

[12] Farge M., Kevlahan N., Bardos C., Schneider K., *Combining deterministic and statistical approaches to compute two-dimensional turbulent flows with walls*; in Trends in Mathematics (Eds. A. Tsinober and A. Gyr), Birkhäuser (1999), pp. 163-174.

[13] Farge M., *Wavelet transforms and their applications to turbulence*; Ann. Rev. Fluid Mech. 24 (1992) pp. 395–457.

[14] Farge M., Schneider K. and Kevlahan N., *Non–Gausianity and Coherent Vortex Simulation for two–dimensional turbulence using an adaptive orthonormal wavelet basis*; Phys. Fluids, 11 (8), (1999) pp. 2187–2201.

[15] Gresho P., Sani R., *Incompressible Flow and the Finite Element Method*; Wiley (1998)

[16] Griebel M., *Adaptive sparse grid multilevel methods for elliptic PDEs based on finite differences*; Computing 61 No. 2 (1998), pp. 151-180;

[17] Griebel M., Knapek S., *Optimized tensor-product approximation spaces*; to appear in Constr. Appr.

[18] Griebel M., Schiekofer T., *An adaptive sparse grid Navier-Stokes solver in 3D based on the finite difference method*, Proceedings of ENUMATH97 (1997)

[19] Griebel M., Oswald P., *Tensor product type subspace splitting and multilevel iterative methods for anisotropic problems*; Adv. Comp. Math. 4 (1995), pp. 171-206

[20] Koster F., *A Proof of the Consistency of the Finite Difference Technique on Sparse Grids*; University Bonn, (2000) preprint

[21] Koster F. Griebel M., *Orthogonal wavelets on the interval*; University Bonn, (1998) SFB 256 report No. 576

[22] Koster F. Griebel M., *An Adaptive Collocation Scheme for the Navier Stokes Equations Using Dubuc-Deslaurier Interpolets* ; University Bonn, (2000) in preparation

[23] Koster F. Griebel M., *Efficient Preconditioning of Linear Systems for the Galerkin, Finite Difference and the Collocation Method on Sparse Grids*; University Bonn, (2000) in preparation

[24] Kröner D., *Numerical Schemes for Conservation Laws*; Wiley-Teubner (1997)

[25] Lesieur M., Staquet, C., Le Roy, P. and Comte P., *The mixing layer and its coherence examined from the point of view of two–dimensional turbulence*; J. Fluid Mech. 192 (1998) 511–535.

[26] Michalke, A., *On the inviscid instability of the hyperbolic tangent velocity profile*; J. Fluid Mech. 19 (1964) 543–556.

[27] Oswald P., *Multilevel Finite Element Approximation*; Teubner Verlag (1994)

[28] Prohl A., *Projection and Quasi Compressibility Methods for Solving the Incompressible Navier Stokes Equations*; Teubner Verlag (1997)

[29] Fröhlich J., Schneider K., *An Adaptive Wavelet-Vaguelette Algorithm for the Solution of PDEs*; J. Compt. Phys. 130 (1997), pp. 174-190

[30] Schneider K. and Farge M., *Wavelet approach for modelling and computing turbulence*; Lecture Series 1998–05 Advances in turbulence modelling, von Karman Institute for Fluid Dynamics, Bruxelles (1998).

[31] Schneider K., Kevlahan N., Farge M., *Comparison of an adaptive wavelet method and nonlinearly filtered pseudo-spectral methods for two-dimensional turbulence*; Theoret. Comput. Fluid Dynamics 9 (1997) pp. 191–206.

[32] Schneider K., Farge M., *Wavelet forcing for numerical simulation of two-dimensional turbulence*; C. R. Acad. Sci. Paris, série II b 325 (1997) 263–270.

[33] Sweldens W., *The lifting scheme: a construction of second generation wavelets*; SIAM J. Math. Anal. 29,2 (1997), pp. 511-546

[34] Temlyakov V., *Approximation of Periodic Functions*; Nova Science Publishers, N.Y. (1993)